

# Environment Matters: CO<sub>2</sub>RR Electrocatalyst Performance Testing in a Gas-Fed Zero-Gap Electrolyzer

María de Jesús Gálvez-Vázquez,<sup>⊥</sup> Pavel Moreno-García,<sup>\*,⊥</sup> Heng Xu, Yuhui Hou, Huifang Hu, Iván Zelocualtecatl Montiel, Alexander V. Rudnev, Shima Alinejad, Vitali Grozovski, Benjamin J. Wiley, Matthias Arenz, and Peter Broekmann\*



Cite This: *ACS Catal.* 2020, 10, 13096–13108



Read Online

ACCESS |



Metrics & More



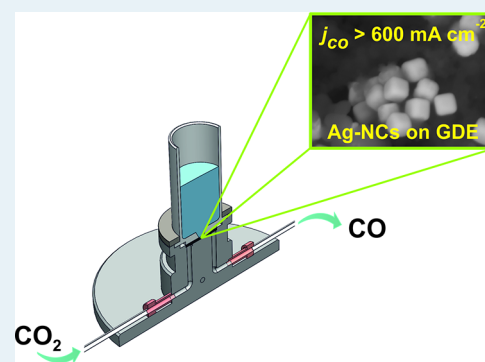
Article Recommendations



Supporting Information

**ABSTRACT:** Among the electrolyzers under development for CO<sub>2</sub> electroreduction at practical reaction rates, gas-fed approaches that use gas diffusion electrodes (GDEs) as cathodes are the most promising. However, the insufficient long-term stability of these technologies precludes their commercial deployment. The structural deterioration of the catalyst material is one possible source of device durability issues. Unfortunately, this issue has been insufficiently studied in systems using actual technical electrodes. Herein, we make use of a morphologically tailored Ag-based model nanocatalyst [Ag nanocubes (NCs)] assembled on a zero-gap GDE electrolyzer to establish correlations between catalyst structures, experimental environments, electrocatalytic performances, and morphological degradation mechanisms in highly alkaline media. The morphological evolution of the Ag–NCs on the GDEs induced by the CO<sub>2</sub> electrochemical reduction reaction (CO<sub>2</sub>RR), as well as the direct mechanical contact between the catalyst layer and anion-exchange membrane, is analyzed by identical location and post-electrolysis scanning electron microscopy investigations. We find that at low and mild potentials positive of  $-1.8$  V versus Ag/AgCl, the Ag–NCs undergo no apparent morphological alteration induced by the CO<sub>2</sub>RR, and the device performance remains stable. At more stringent cathodic conditions, device failure commences within minutes, and catalyst corrosion leads to slightly truncated cube morphologies and the appearance of smaller Ag nanoparticles. However, comparison with complementary CO<sub>2</sub>RR experiments performed in H-cell configurations in a neutral environment clearly proves that the system failure typically encountered in the gas-fed approaches does not stem solely from the catalyst morphological degradation. Instead, the observed CO<sub>2</sub>RR performance deterioration is mainly due to the local high alkalinity that inevitably develops at high current densities in the zero-gap approach and leads to the massive precipitation of carbonates which is not observed in the aqueous environment (H-cell configuration).

**KEYWORDS:** CO<sub>2</sub> electroreduction, gas diffusion electrodes, zero-gap electrolyzer, carbon monoxide, exchange membrane electrode assembly



## INTRODUCTION

Powering the electrochemical reduction reaction of carbon dioxide (CO<sub>2</sub>RR) with renewable energy sources has emerged as a compelling alternative to other approaches to CO<sub>2</sub> valorization,<sup>1,2</sup> toward meeting the increasing demand for commodity/platform chemicals and thereby contributing to efforts to close the anthropogenic carbon cycle.<sup>3,4</sup> In recent decades, significant progress has been made to understand the reaction mechanisms of this process through the development of cutting-edge catalyst materials that increase the activity [partial current density (PCD) of generated products] and selectivity (faradaic efficiency, FE) of the process. Strong cases of commercial viability have been made for formate (HCOO<sup>-</sup>) and CO production, which require the transfer of only two electrons from the electrocatalyst to the CO<sub>2</sub> reactant molecule.<sup>5,6</sup> Formate is efficiently formed on Sn-, Bi-, In-, and Pb-based catalysts, whereas CO forms preferably on Ag-,

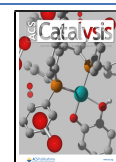
Au-, and Zn-based catalysts.<sup>7</sup> CO is a particularly appealing product because it can be used as a stockpile for subsequent transformation either in the Fischer–Tropsch process<sup>8</sup> or in sequential electrochemical<sup>9</sup> and fermentation methods.<sup>10</sup>

Using catalyst screening methods based on H-cell experiments in which reactant CO<sub>2</sub> gas is usually dissolved in an aqueous bicarbonate-based electrolyte, a significant number of works have reported that Ag,<sup>11–13</sup> Au,<sup>14,15</sup> and Zn-based<sup>16–18</sup> cathode materials provide excellent CO selectivity and

Received: August 18, 2020

Revised: October 15, 2020

Published: October 27, 2020



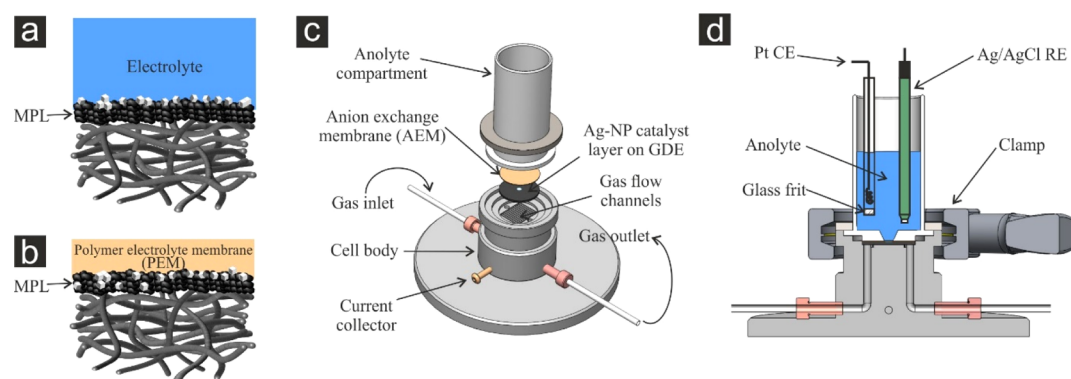


**Figure 1.** Schematics of the reaction interfaces in (a) liquid flow-cell electrolyzer and (b) exchange membrane electrode assembly (MEA) or zero-gap assembly. (c) Depiction and assembly of the zero-gap flow cell used in this work for the CO<sub>2</sub>RR. (d) Cross-sectional view of the assembled cell with reference and counter electrodes (CE and RE, respectively) immersed in the anolyte compartment. MPL in panels (a,b) stands for the MPL on which the catalyst material (Ag-NCs) is embedded.

operational stability. Many works have also reported insightful correlations between the use of a tailored catalyst nanostructure and electrocatalytic performance.<sup>19,20</sup> In addition, diverging from the bicarbonate-based electrolyte that was once used almost ubiquitously, it has been found that highly concentrated (potassium) hydroxide-based catholyte solutions suppress the parasitic hydrogen evolution reaction (HER) and improve the CO<sub>2</sub>RR performance because OH<sup>-</sup> ions exhibit excellent ionic conductivity and reduce the activation energy barriers for CO<sub>2</sub> electroreduction.<sup>9,21–24</sup> Through these and other improvements, the field has reached a significant level of maturity so that currently, the associated research is driven by more ambitious endeavors, namely, scaling up the CO<sub>2</sub>RR process to practical realization.<sup>10,25</sup> Toward this end, experimental platforms have been developed to circumvent or attenuate the mass transport limitations that are intrinsic to traditional H-type cell measurements<sup>26–28</sup> and arise from the low solubility of the dissolved CO<sub>2</sub> reactant in aqueous electrolytes. This pursuit opens a new avenue to the CO<sub>2</sub>RR and related fields because the insights extracted from H-cell measurements with either stationary or rotating disk electrodes do not necessarily hold for their gas-fed homologues and both approaches bear fundamental kinetic differences that must be addressed to approach process commercialization.<sup>29–31</sup>

Among the various types of CO<sub>2</sub> electrolyzers under development, gas-fed approaches that use gas diffusion electrodes (GDEs) as cathodes and that are inspired by polymer electrolyte fuel cell technologies are considered to be the most promising.<sup>1,21,30,32–36</sup> Consequently, studies on Ag-GDEs in contact with flowing alkaline electrolytes (Figure 1a) have grown in popularity to achieve higher PCD<sub>CO</sub> and FE<sub>CO</sub> values as well as lower CO<sub>2</sub>RR onset potentials and to explore possible enhancements to performance longevity.<sup>37–41</sup> However, electrolyzer designs that rely on this cell configuration are not without shortcomings that affect device performance and stability, thereby overshadowing their intrinsic electrocatalytic activity. These issues stem from (i) high ohmic losses owing to the electrolyte layer separating the electrodes,<sup>30</sup> (ii) electrolyte percolation through the microporous layer (MPL) of GDEs and concomitant carbonate salt precipitation,<sup>42,43</sup> and (iii) CO<sub>2</sub> crossover from the cathodic to the anodic compartment upon CO<sub>2</sub> neutralization by OH<sup>-</sup> ions to HCO<sub>3</sub><sup>-</sup>/CO<sub>3</sub><sup>2-</sup>.<sup>32,44,45</sup>

Motivated by this, a few recent works on alternative cell designs with only an aqueous anolyte between the membrane

and anode and no liquid electrolyte layer between the catalyst layer and (an)ion-exchange membrane [indistinctly called exchange membrane electrode assemblies (MEAs) or catholyte-free or zero-gap membrane assemblies, see Figure 1b]<sup>1,32,46</sup> have been reported, enabling comparably reduced ohmic overpotentials, enhanced stability, and excellent CO selectivity.<sup>25,47,48</sup> This zero-gap configuration not only affords reduced ohmic losses but also attenuates complications that arise from poor membrane hydration and electrode flooding at high current densities, which are otherwise problematic to fully gas-fed electrolyzers<sup>46,49</sup> (note that exchange MEA electrolyzers may still suffer from the parasitic uptake of CO<sub>2</sub> at the interface of the cathode and anion-exchange membrane, thus facilitating the undesirable CO<sub>2</sub> discharge on the anode surface).<sup>43,44,50</sup> Nonetheless, one persistent hurdle that precludes the commercial deployment of these technologies is insufficient long-term device stability, which continues to fall short of the minimum target value of 8 × 10<sup>4</sup> h.<sup>5</sup> Efforts to identify the factors that lead to process failure have been undertaken, and strategies to alleviate such failures have been proposed (e.g., appropriate selection of the reactor design, electrode production method and hydrodynamics,<sup>1</sup> management of electrolyte percolation through the GDE,<sup>39,51</sup> and carbonation tolerance of the electrodes<sup>43,44</sup>).

In this context, another aspect that may also be a source of device durability issues and that has been minimally investigated using actual technical electrodes on which very large current densities (>300 mA cm<sup>-2</sup>) are enforced is the structural deterioration of the catalyst material.<sup>31,40</sup> In particular, studies of the catalyst morphological evolution of Ag-based exchange MEAs induced by the CO<sub>2</sub>RR reaction itself are lacking, as well as studies of the effect of direct mechanical contact between the catalyst layer and anion-exchange membrane (Figure 1b). To shed light on this unexplored aspect of CO<sub>2</sub>RR on Ag-GDEs, we make use of morphologically tailored Ag-based model nanocatalysts [Ag nanocubes (Ag-NCs)] assembled on zero-gap GDEs to establish correlations between structure, environment, electrocatalytic performance, and degradation mechanisms under the abovementioned most favorable CO<sub>2</sub>RR conditions (i.e., a highly alkaline membrane adjacent to the catalyst layer). Sub-monolayer surface coverages are purposely employed to unambiguously address possible structure degradation at the level of a single Ag-NC. Besides investigation of the catalyst activity and selectivity, we devote particular attention to the

time evolution of both the electrochemical performance of the process and the material's nanostructure induced upon CO<sub>2</sub> electrolysis at large current densities, as enforced on the model exchange Ag–MEAs. We find that our testbed enables among the highest CO partial current densities and competitive FE<sub>CO</sub> values (−625 mA cm<sup>−2</sup> and 85%, respectively) even at the applied sub-monolayer catalyst coverages. Two distinct electrode potential regimes were observed, each exhibiting significantly different behaviors. At low and mild applied potentials ( $E \geq -1.8$  V vs Ag/AgCl), stability prevails across the PCD<sub>CO</sub> and FE<sub>CO</sub>, electrolyzer performance, and catalyst structure. Conversely, at greater cathodic potentials, the process selectivity and activity severely degrade, leading to performance failure even though the catalyst morphology undergoes significantly less deterioration. Thus, this work enables the deconvolution of catalyst structural stability from system performance stability. Finally, a comparison with standard H-type reference measurements reveals that CO<sub>2</sub>RR product selectivity is influenced by electrolyzer design and, therefore, that the knowledge developed using such batch-type approaches should not be regarded as directly transferable to gas-fed platforms. Overall, the results underscore that more effort must be devoted to the understanding and optimization of system design parameters (e.g., water management, prevention of salt precipitation, CO<sub>2</sub> flow rate, and electrolyte flow rate) that have a more significant impact on the product spectrum and longevity of the exchange MEA electrolyzers than that of the structural degradation of the catalyst, which is shown to be mild.

## ■ EXPERIMENTAL SECTION

**Synthesis of Ag–NCs.** Silver NCs were synthesized using a previously reported method with minor modification.<sup>52</sup> 5 mL of ethylene glycol (EG, J. T. Baker) was added to a 250 mL two-neck flask preheated to 160 °C. A light N<sub>2</sub> flow was introduced just above the EG for the first 10 min, followed by heating the solvent for another 50 min. Next, 3 mL EG solution of AgNO<sub>3</sub> (94 mM) and 3 mL EG solution containing polyvinylpyrrolidone (PVP,  $M_w = 55,000$ , 144 mM) and NaCl (0.22 mM) were simultaneously injected into the flask at a rate of 45 mL/h, with the solution observed to turn yellow during this process. Under continuous stirring at 160 °C, the solution exhibited a color transition series from yellow to clear yellow, brown, greenish, and finally ochre and opaque. The whole process required 16 h to 24 h for completion. After the solution had turned opaque, the reaction was quenched by adding 22 mL of acetone to the hot solution, followed by cooling in an ice-water bath. To purify the NCs, the solution was first centrifuged at 2000g for 30 min, and then, the precipitate was dispersed and centrifuged 3× in 10 mL of deionized water at 9000g for 10 min per run.<sup>53</sup> The product was finally dispersed in 5 mL of deionized water for future use.

**Preparation of Ag–NC Catalyst Ink.** To prepare the carbon-supported Ag–NC ink, 1.5 mg of the prepared Ag–NCs and 0.26 mg of carbon black (Vulcan XC 72R, Cabot) were separately dispersed in 10 mL of isopropanol (VLSI Selectipur, BASF SE, Ludwigshafen, Germany) by 1 h of sonication. Both suspensions were intermixed, sonicated for 1 h, and dried using a Rotary evaporator (Buchi R210, 45 °C, 85 mbar). The obtained carbon-supported Ag–NCs (85 wt % Ag–NC and 15 wt % C black) were then redispersed in 1 mL of isopropanol containing 50 μL of Nafion (5 wt %, 15–20% water, Sigma-Aldrich). The resulting suspension was subjected

to sonication for 1 h yielding a homogeneous catalyst ink. For the sake of reproducibility and comparison, catalyst inks were also prepared with commercial Ag–NCs (NanoXact, nano-Composix) and used for complementary CO<sub>2</sub>RR experiments.

**Preparation of the Ag–NC–GDEs.** The model catalyst material in this work consists of cubic Ag nanoparticles (Ag–NCs) with an average edge length of (113.1 ± 10.6) nm. The Ag–NC–GDEs for all electrochemical and characterization experiments were prepared as follows: a defined circular area of 7.07 × 10<sup>−2</sup> cm<sup>2</sup> on the GDEs' hydrophobic surface (diameter of 2 cm, Sigracet 39 BC, Fuel Cell Store) was modified by dropcasting 50 μL of carbon-supported Ag–NC ink onto its top surface. This catalyst solution was percolated through the porous body of the GDEs by a vacuum filtration system placed on the backside of the electrode, and subsequent drying at ambient conditions was allowed for at least 30 min. Analysis by inductively coupled plasma–mass spectrometry (ICP–MS) of freshly prepared samples was used to determine the catalyst mass loading, which amounted to ~7.1 × 10<sup>−2</sup> mg<sub>Ag</sub> cm<sup>−2</sup>.

**Assembly of the Gas Flow Cell.** The assembly and main components of the zero-gap gas-flow cell employed in this work to investigate correlations between the catalyst structure and process performance of CO<sub>2</sub>RR to CO on Ag–NC–GDEs are schematically depicted in Figure 1c,d. This assembly consists of a stainless-steel cell body with the gas flow channels used to feed the CO<sub>2</sub> from the backside of the prepared Ag–NC–GDEs mounted on the outermost location of the central portion. Other components incorporated into the cell include a current collector and a gas inlet and outlet to control the supply of the CO<sub>2</sub> reactant (99.999%, Carbagas, Switzerland) and analysis of the gaseous products, respectively. All CO<sub>2</sub>RR experiments were set up by placing a freshly prepared Ag–NC–GDE on top of the gas flow channels, with its catalyst-modified surface facing upward. Subsequently, a clean hydroxide-functionalized Sustainion alkaline membrane (X37-50 RT, Dioxide materials) and a poly(tetrafluoroethylene) (PTFE) anolyte compartment were carefully placed on top of the Ag–NC–GDE. A clamp was then used to ensure cell tightness and mechanical stability. KOH electrolyte-supporting solution (10 mL, 2 M; pH: 14.3, Sigma-Aldrich) was added to the anolyte compartment, and a Ag/AgCl (3 M KCl, double junction design, Metrohm) electrode and a Pt mesh (99.99%, MaTeck) separated by a glass frit served as the reference and counter electrodes, respectively. Note that the PTFE anolyte compartment has a central orifice (7.07 × 10<sup>−2</sup> cm<sup>2</sup>) in its bottom part that provides direct contact between the electrolyte and the underlying anion-exchange membrane, while the Ag–NC–GDE is prevented from establishing physical contact with the supporting anolyte. During electrolysis, a humidified CO<sub>2</sub> stream (16 mL min<sup>−1</sup>) was continuously fed through the gas flow channels of the stainless-steel cell body adjacent to the prepared Ag–NC–GDEs.

**Electrochemical Reduction of CO<sub>2</sub> (CO<sub>2</sub>RR) Using Ag–NC–GDEs.** All electrolytes were prepared using chemicals of at least ACS reagent grade and deionized water (Millipore, 18.2 MΩ cm, 3 ppb toc). Both ECi-200 (Nordic electrochemistry) and Autolab PGSTAT128 N (Metrohm) potentiostats were used to perform all electrochemical experiments. Electrochemical impedance spectroscopy measurements were conducted before and after every CO<sub>2</sub> electrolysis experiment, and the results were considered to build the potential-dependent product distributions and partial current densities displayed and mentioned throughout the text. Potentiostatic

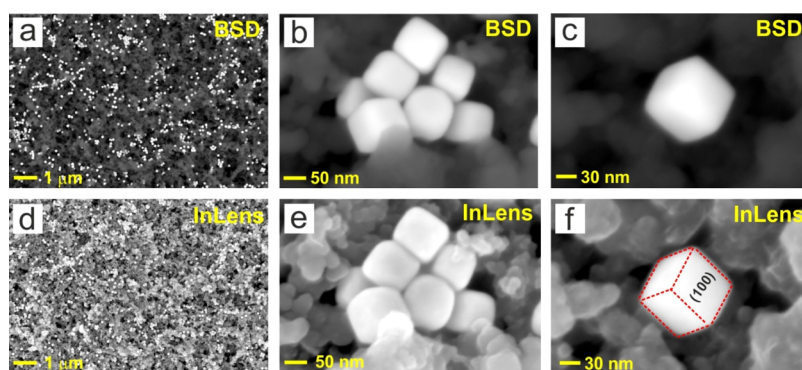


**Figure 2.** Representative SEM images at different magnifications showing the surface of an as-prepared Ag-NC-GDE cathode for CO<sub>2</sub>RR. (a,d) Ag-NC catalyst sub-monolayer coverage on the MPL of the GDE. (b,c) and (e,f) reveal the well-defined cubic morphology of the Ag-NCs. Images (a–c) were acquired using the BSD detector of the scanning electron microscope. (d–f) Correspond to the same sample surface areas shown in the upper panels but were recorded with the InLens SE detector.

CO<sub>2</sub> electrolysis experiments were carried out at selected applied electrode potentials for 1 h, during which time the electrogenerated gaseous products were analyzed by online gas chromatography (SRI Instruments) in sequential intervals of 10 min. The electrolyte was analyzed after the applied electrolysis condition (post reaction) to quantify the produced formate by means of ion-exchange chromatography (Metrohm Ltd., Switzerland). For comparison, the performance of the Ag-NC-GDEs was also tested by dedicated reference measurements using 2 M KHCO<sub>3</sub> as the electrolyte in both the gas-flow cell and the conventional H-cell configurations. For the H-cell measurements, a proton-exchange membrane (Nafion 117, Sigma-Aldrich) separated the catholyte from the anolyte, and the working electrode consisted of a rectangular piece of carbon paper (0.8 × 3 cm) prepared in the same way as the Ag-NC-GDEs for zero-gap measurements. The back side and the edges of these electrodes were masked with the PTFE tape, thus leaving an uncovered geometric surface area of 0.2 cm<sup>2</sup>. A single junction Ag/AgCl electrode (saturated KCl, Pine Research) and a Pt foil (2.5 × 0.8 cm, 99.99%, MaTeck) were used as the reference and counter electrodes, respectively. All electrode potential values in this work are in reference to the standard Ag/AgCl<sub>3M</sub> reference electrode. The data corresponding to the product selectivity and partial current densities of all experiments are displayed in Tables S2–S6. A thorough description of complementary experimental details is presented in a previous publication.<sup>36</sup>

**Scanning Electron Microscopy and Energy-Dispersive X-ray Spectroscopy Characterization.** Morphological characterization of the prepared Ag-NC-GDEs and assessment of the spatial distribution of the Ag-NCs over the samples was carried out with scanning electron microscopy (SEM) imaging experiments. Imaging was performed before (for the as-prepared electrodes) and after having sustained defined CO<sub>2</sub>RR time intervals at selected applied electrode potentials. The analysis was conducted sequentially with a Zeiss Gemini 450 scanning electron microscope with both InLens secondary electron and backscattered electron detectors (InLens SE and BSD detectors, respectively). An accelerating voltage of 5 kV and a current of 200 pA were applied at a working distance of 6.6–6.8 mm. The BSD detector enables clear identification of the Ag-NCs along the surface of the GDE's MPL because this technique is highly sensitive to the atomic number of the elements being imaged. However, the images acquired with the InLens SE detector

provide better morphological resolution of the Ag-NCs. The use of both imaging operational modes coupled to energy-dispersive X-ray analysis (EDX) analysis made it possible to track morphological catalyst changes induced by CO<sub>2</sub> electrolysis and/or physical contact between the catalyst material and anion-exchange membrane on the Ag-NC-GDEs used. Complementary identical location (IL-SEM) experiments were conducted on Ag-NC-GDEs for which selected sample positions were imaged by the SEM instrument before and after CO<sub>2</sub>RR experiments.

AZtec 4.2 software (Oxford Instruments) was used to acquire EDX spectra and surface mappings of selected Ag-NC-GDEs. An acceleration voltage of 10 kV and a current of 1.2 nA were applied at a working distance of 8.5 mm.

**Catalyst Loading and Post-electrolysis Electrolyte and Ag-NC-GDE Analysis by ICP-MS.** Freshly prepared Ag-NC-GDEs were immersed in 3 mL HNO<sub>3</sub> (BASF SE, Ludwigshafen, Germany) for 24 h to dissolve the Ag-NCs embedded on their surfaces. The resulting solutions were diluted with 3% HNO<sub>3</sub> solution by a factor of 500 and were then fed into a NEXION 2000 ICP-MS instrument (PerkinElmer) to obtain the Ag mass loading of the electrodes. To identify possible Pt dissolution from the employed Pt counter electrode during CO<sub>2</sub> electrolysis, the following ICP-MS and EDX control experiments were conducted. First, 10 μL of post-reaction anolyte (after CO<sub>2</sub>RR at –2.0 V for 60 min in 2 M KOH) was diluted with 10 mL of 3% HNO<sub>3</sub> solution for ICP-MS analysis. No Pt dissolution was detected in two independent measurements. Additionally, two post-electrolysis Ag-NC-GDEs were immersed in 3 mL aqua regia for 24 h and the solutions were diluted by factor 100 with 3% HNO<sub>3</sub>. The corresponding ICP-MS spectra showed no signal other than the background further confirming the absence of Pt on the catalyst surface and supporting GDE. Finally, EDX analysis of a Ag-NC-GDE sample after being subjected to similar CO<sub>2</sub>RR conditions also excluded the presence of any Pt deposited on the employed cathodes (see Figure S8).

**X-ray Diffraction Catalyst Characterization.** The crystallinity of the Ag-NCs was determined by means of X-ray diffraction (XRD) techniques (Bruker D8) using Cu K $\alpha$  radiation ( $\lambda = 0.1540$  nm, 40 mA) generated at 40 keV. Scans were recorded at 1° min<sup>–1</sup> for 2 $\theta$  values between 20 and 100°. The samples were prepared by dropcasting Ag-NCs dispersed in isopropanol on a graphite foil (0.13 mm, 99.8%, Alfa Aesar) and then allowing the solution to dry under ambient

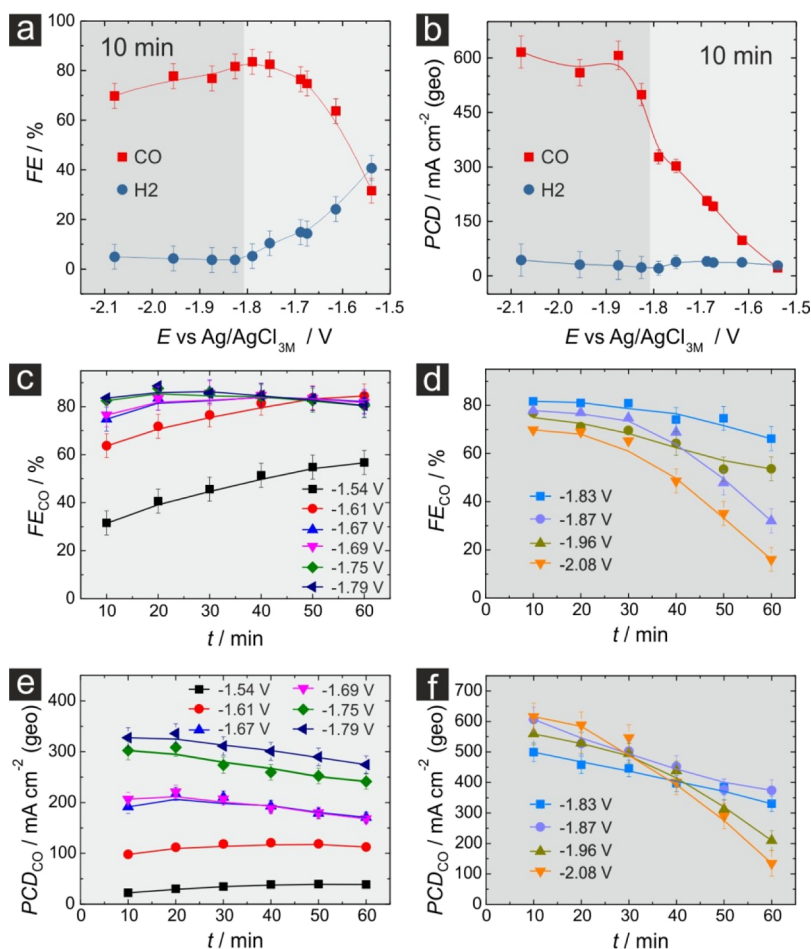


**Figure 3.** Potential-dependent FEs (a) and PCDs (b) of the gaseous products obtained from CO<sub>2</sub>RR on the gas-fed Ag–NC–GDEs 10 min after beginning CO<sub>2</sub> electrolysis. Time evolution of the FE<sub>CO</sub> at (c) mild (–1.5 V > E > –1.8 V) and (d) high applied potentials (–1.83 V > E > –2.1 V). Corresponding time evolution of the PCD<sub>CO</sub> at mild (e) and high (f) applied potentials. All experiments were carried out using 2 M KOH in the anolyte compartment. The solid lines in all panels are guides to the eye to better observe the trends. The experimental error was accounted for using ±5% error bars.

conditions. The obtained XRD patterns were analyzed and compared with JCPD (Joint Committee on Powder Diffraction) for peak assignment.

## RESULTS AND DISCUSSION

**Characterization of Ag–NC–GDEs by SEM.** Figure 2 shows representative SEM images of an as-prepared Ag–NC–GDE. We present data acquired sequentially at the same position with both the BSD and InLens SE detectors of the scanning electron microscope. Clear distinction between the Ag–NCs (bright) and the supporting GDE (dark) is provided by the BSD detector, which is sensitive to the atomic number of the analyzed material (Figure 2a–c). We observe a highly dispersed sub-monolayer of Ag–NC surface coverage built up by both single Ag–NCs and sparse groups of the particles (Figure 2b,c). This observation implies that the electrochemical performance of the Ag–NC–GDEs will be partially determined by parasitic side reactions (e.g., HER) taking place also on catalyst-free regions. This is supported by the combined SEM–EDX analysis of an as-prepared Ag–NC–GDE sample displayed in Figure S1a–d. The images acquired using the InLens SE detector (Figure 2d–f) offer improved morphological resolution of single Ag–NCs and their cubic shape, which is more easily observed at large magnifications

(Figure 2e–f). Statistical analysis of more than 400 Ag–NCs provided an average edge length of  $113.1 \pm 10.6$  nm, while XRD characterization confirmed the high crystallinity of the assembled Ag–NCs (Figure S1e,f). Recent theoretical and experimental studies in H-cell configurations have reported the superior and stable catalytic performance of cubic Ag nanoparticles compared to their octahedral and spherical counterparts.<sup>19,20</sup>

**Electrocatalytic Performance of Ag–NC–GDEs for CO<sub>2</sub>RR in Zero-Gap Electrolyzer.** Potentiostatic CO<sub>2</sub>RR experiments at selected applied potentials ranging between –1.55 and –2.1 V versus Ag/AgCl were conducted for 1 h using a dedicated Ag–NC–GDE as the cathode in a zero-gap gas flow-cell configuration (Figure 1b–d) for every potential. A favorable alkaline reacting environment was provided by the 2 M KOH electrolyte used in the anolyte compartment.<sup>42</sup> Figure 3a displays the potential-dependent product distribution of the gaseous products obtained after 10 min of CO<sub>2</sub> electrolysis. Besides the modest FE<sub>CO</sub> observed at E ~ –1.55 V, all obtained FE<sub>CO</sub> values at potentials more negative than –1.6 V surpassed 65%, reaching a maximum value of approximately 85% at –1.8 V. Diverging from previous reports in which an abrupt decay of FE<sub>CO</sub> was observed with progressively higher potentials/current densities, only a slight decrease of CO

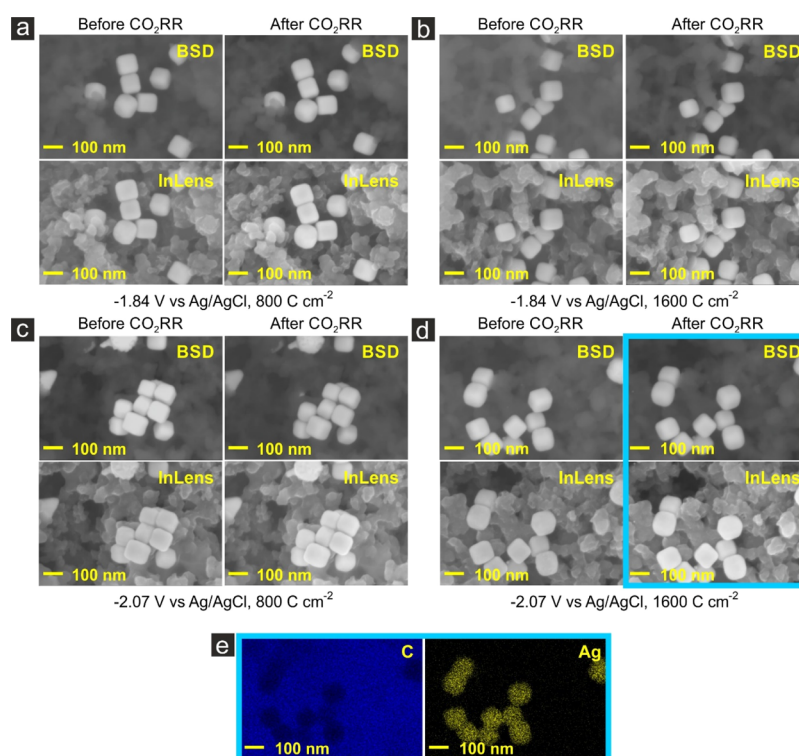


**Figure 4.** Representative IL-SEM images of Ag-NC-GDE cathode surfaces before and after having conducted dedicated gas-fed CO<sub>2</sub>RR experiments at  $-1.84$  V for (a) 30 min ( $800 \text{ C cm}^{-2}$ ) and (b) 60 min ( $1600 \text{ C cm}^{-2}$ ) and at  $-2.07$  V for (c) 13 min ( $800 \text{ C cm}^{-2}$ ) and (d) 32 min ( $1600 \text{ C cm}^{-2}$ ) captured using both BSD and InLens SE detectors. (e) Elemental EDX mappings showing the spatial distribution of C (dark blue) and Ag (yellow) corresponding to the sample location highlighted by the blue rectangle in (d). All CO<sub>2</sub>RR experiments were carried out using 2 M KOH in the anolyte compartment.

selectivity was detected at the harshest applied cathodic conditions due to an emerging formate contribution. However, it should be noted that in those previous reports either a bipolar membrane or a 0.5 M KHCO<sub>3</sub> buffer layer was used between the cathode and proton-exchange membrane.<sup>32,54,55</sup> The efficiency of parasitic H<sub>2</sub> stayed at FE<sub>H<sub>2</sub></sub> levels  $\leq 10\%$  for potentials more negative than  $-1.75$  V. The corresponding dependence of the partial current densities PCD<sub>CO</sub> and PCD<sub>H<sub>2</sub></sub> on the enforced potentials is shown in Figure 3b. The PCD<sub>CO</sub> increases steeply as the cathodic potential increases from  $-1.54$  to  $-1.87$  V reaching highly competitive levels at approximately  $-600 \text{ mA cm}^{-2}$  (see Table S1). Further cathodic polarization to approximately  $-2.1$  V leads to a slightly increased PCD<sub>CO</sub> reaching approximately  $-625 \text{ mA cm}^{-2}$ . The PCD<sub>H<sub>2</sub></sub> did not exceed  $-50 \text{ mA cm}^{-2}$  at all applied potentials. These CO selectivities and partial current densities stand out considering that for the as-prepared Ag-NC-GDEs, a significant portion of the three-phase boundary layer where the fed CO<sub>2</sub>, polymer electrolyte, and catalyst material meet is constituted by the unmodified MPL of the support GDEs (Figure 2a). Clearly, an increase of the catalyst loading would lead to even better CO efficiencies and activities.<sup>31</sup> However, it is important to remember that a low catalyst surface coverage on the GDEs was deliberately applied to successfully monitor the morphological evolution of the Ag-NC catalyst at the single nanoparticle level (see below).

Distinct temporal evolution of both FE<sub>CO</sub>s and PCD<sub>CO</sub>s was found to depend on the magnitude of the applied potentials. Based on the temporal stability that these values promoted, two apparent potential regimes were identified for FE<sub>CO</sub> and PCD<sub>CO</sub>. These regimes are highlighted by different color codes

in Figure 3. The panels corresponding to applied potentials that sustained the above-described performance throughout the duration of the experiments are highlighted by light gray rectangles ( $-1.5 \text{ V} > E > -1.8 \text{ V}$ ). The panels highlighted in darker gray stand for results derived from applied potentials that led to the decay of FE<sub>CO</sub> and PCD<sub>CO</sub> values from their initial levels. Figure 3 panels c and e show that both CO selectivity and activity either improve or stay fairly stable across the lifespan of the experiments, provided that the applied potential was always less negative than  $-1.8$  V. Conversely, when the potential surpassed this value, both CO production figures decreased over time. This decline was initially mild but intensified abruptly after 30 min with an increase of the applied potential (Figure 3 panels d and f).

#### Morphology Evolution of Ag-NC-Based Catalyst Induced by CO<sub>2</sub>RR in Zero-Gap Flow Cell and H-Type Cell.

To determine whether the observed decay in device performance during CO<sub>2</sub>RR at the specific time intervals and applied potentials observed in Figure 3 panels d and f arises from morphological transformations of the cathodes (through morphological changes of the Ag-NCs or through their local rearrangement along the GDE surface), we analyzed Ag-NC-GDEs that were used for CO<sub>2</sub>RR under those same conditions using *ex situ* SEM imaging experiments. Note that in the present study, our Ag-NC catalyst was subjected to significantly harsher cathodic conditions as compared to those reported in ref 61 reaching over two orders higher current densities and  $\sim 400$  mV more cathodic potentials.

In the first attempt, we employed the so-called IL-SEM-based technique.<sup>56,57</sup> This analysis is meant to provide the structural evolution of electrocatalyst materials by comparing

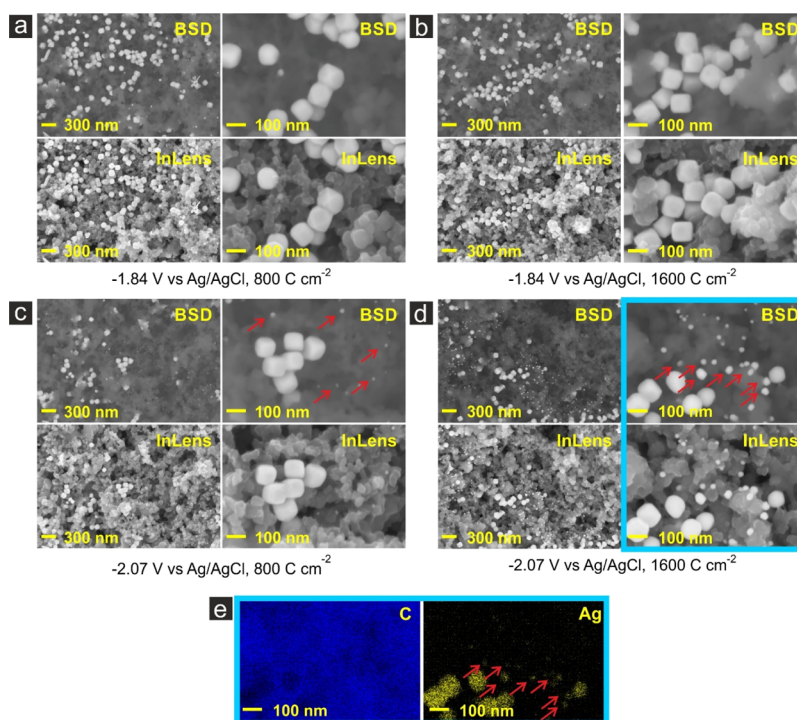


**Figure 5.** Representative SEM images of Ag-NC-GDE cathode surfaces after having conducted dedicated gas-fed CO<sub>2</sub>RR experiments at  $-1.84$  V for (a) 30 min ( $800 \text{ C cm}^{-2}$ ) and (b) 60 min ( $1600 \text{ C cm}^{-2}$ ) and at  $-2.07$  V for (c) 13 min ( $800 \text{ C cm}^{-2}$ ) and (d) 32 min ( $1600 \text{ C cm}^{-2}$ ) captured using both BSD and InLens SE detectors. (e) Elemental EDX mappings showing the spatial distribution of C (dark blue) and Ag (yellow) of the sample location highlighted by the blue rectangle in (d). Red arrows identify Ag nanoparticles formed upon cathodic corrosion of the Ag-NC catalyst. All CO<sub>2</sub>RR experiments were carried out using 2 M KOH in the anolyte compartment.

their morphology at the same sample location before and after being subjected to electrolysis.<sup>56,57</sup> We have previously employed this strategy to successfully assess structure-activity correlations caused by CO<sub>2</sub>RR on bare porous metal electrocatalysts.<sup>17,58</sup> Herein, we monitored the structural evolution of Ag-NC-GDEs by IL-SEM for samples that were subjected to high cathodic potential values at which CO partial current densities reached  $-500 \text{ mA cm}^{-2}$  and  $-620 \text{ mA cm}^{-2}$  ( $-1.84$  and  $-2.07$  V, respectively). For each applied potential, the electrolysis was carried out until charge densities of  $800$  and  $1600 \text{ C cm}^{-2}$  were passed on dedicated Ag-NC-GDEs. These selected conditions are key for enabling insightful correlation between the SEM-based post-electrolysis studies and the data presented in Figure 3c-f.

Figure 4a-d presents representative IL-SEM images corresponding to Ag-NC-GDEs that were subjected to such CO<sub>2</sub>RR conditions. Surprisingly, comparison of SEM images acquired before and after CO<sub>2</sub> electrolysis show that neither detachment nor degradation of the Ag-NCs seem to arise regardless of the specific applied potential, passed charge, or electrolysis duration. Post-electrolysis EDX mappings on sample regions that were scrutinized by IL-SEM also hint at the absence of cathodic corrosion and redeposition phenomena (compare Figures 4e and S1b,d). Furthermore, complementary IL-SEM experiments in which five sequential CO<sub>2</sub>RR cycles were applied to a Ag-NC-GDE sample at the most stringent cathodic conditions are displayed in Figure S2. Although this sample was electrochemically stressed more severely (total cumulated  $Q = 13306 \text{ C cm}^{-2}$  and  $t \sim 4.5$  h), the combined IL-SEM-EDX analysis showed again no apparent sample degradation. These results alone would imply, at first sight, that the developed Ag-NC-GDEs tested

in the proposed zero-gap flow cell do not undergo morphological degradation upon CO<sub>2</sub>RR at all and that the undermined catalytic performance observed in Figure 3 at harsh cathodic conditions should originate from another failure source. However, an important aspect that did not need consideration in our previously reported IL-SEM structural CO<sub>2</sub>RR studies and that can be the source of SEM imaging misinterpretation when studying colloidal nanocatalysts is the influence of surfactants that are left behind on their surfaces following their synthesis. Indeed, it has been shown that electron beam irradiation on nanomaterials synthesized by additive-assisted colloidal methods can lead to their improved structural stability through transformation of the adsorbed surfactants into dense carbonaceous shells.<sup>59</sup> Moreover, local surface passivation induced by SEM imaging has been identified on PVP-capped Ag NCs that hinders diffusion of Ag surface atoms.<sup>60</sup> This suggests that IL-SEM experiments might not accurately reveal the morphological evolution of colloidal catalyst materials as the initial electron irradiation conducted before the electrolysis step stabilizes and deactivates the scrutinized locations. Therefore, a second series of SEM imaging experiments were performed on the surface of Ag-NC-GDEs that were subjected to the same CO<sub>2</sub>RR conditions as shown in Figure 4 but whose surfaces were not exposed to the electron beam of the SEM prior to the electrolysis.

Figure 5a-b displays representative images of Ag-NC-GDEs after having been subjected to  $-1.84$  V. The Ag-NCs in panels a and b have undergone insignificant morphological changes after either 30 or 60 min of electrolysis ( $800 \text{ C cm}^{-2}$  and  $1600 \text{ C cm}^{-2}$ , respectively). Furthermore, the images acquired with the BSD detector revealed the absence of

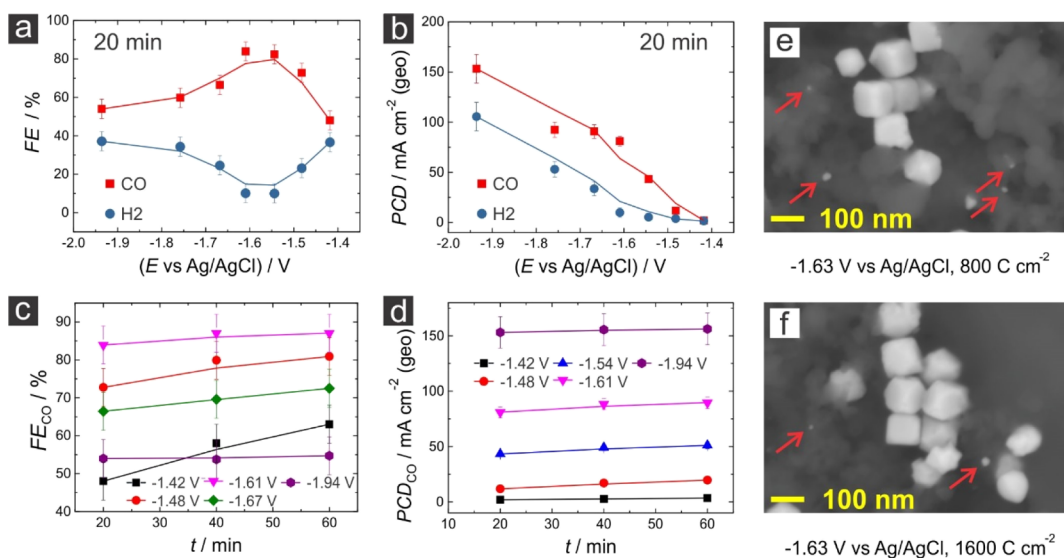


**Figure 6.** Potential-dependent FEs (a) and PCDs (b) obtained on the Ag-NC-GDE in the H-cell configuration. Both variables were recorded 20 min after the CO<sub>2</sub> electrolysis experiment was initialized. Time evolution of the FE<sub>CO</sub> (c) and PCD<sub>CO</sub> (d) at ( $-1.42 \text{ V} \geq E \geq -1.94 \text{ V}$ ). Representative SEM images of cathode surfaces after having conducted dedicated CO<sub>2</sub>RR experiments at  $-1.63 \text{ V}$  for (e) 196 min ( $800 \text{ C cm}^{-2}$ ) and (f) 304 min ( $1600 \text{ C cm}^{-2}$ ). Complementary SEM images of cathode surfaces subjected to  $-1.92 \text{ V}$  are shown in Figure S6. These CO<sub>2</sub>RR experiments were carried out with an H-type cell using 2 M KHCO<sub>3</sub> as the electrolyte. The solid lines in panels (a–d) are guides to the eye to better observe the trends. The experimental error was accounted for using  $\pm 5\%$  error bars.

material removal from the Ag-NCs that would be redeposited in the form of smaller nanoparticles along the electrode surface under the applied cathodic conditions.<sup>61</sup> Importantly, excellent electrochemical performance figures ( $\text{PCD}_{\text{CO}} \geq 300 \text{ mA cm}^{-2}$  and  $\text{FE}_{\text{CO}} \sim 80\%$ ) are attained and sustained if the potential remains just positive of this applied value ( $-1.8 \text{ V vs Ag/AgCl}$ , see Figure 3 panels c and e). Because of the morphological integrity of the actual catalyst observed under these conditions, it is reasonable to think that the purely electrochemical performance of the Ag-NCs-GDEs should be sustained over long electrolysis periods if the other system parameters do not lead to failure (e.g., salt precipitation, electrolyte penetration into the adjacent GDE, etc). However, diverging from what was observed in IL-SEM analysis, the electrodes exposed to more demanding cathodic conditions revealed alteration of the Ag-NC structure that may be linked to the deterioration of  $\text{PCD}_{\text{CO}}$ s and  $\text{FE}_{\text{CO}}$ s observed in Figure 3 panels d and f. Figure 5c shows representative images of a Ag-NC-GDE cathode that underwent CO<sub>2</sub>RR at  $-2.07 \text{ V}$  for 13 min ( $800 \text{ C cm}^{-2}$ ). Although the Ag-NCs maintained their overall cubic appearance, the BSD-SEM images reveal smaller, randomly distributed Ag nanoparticles ( $< 5 \text{ nm}$ ) that arise from these more stringent CO<sub>2</sub> electrolysis conditions. The red arrows in the upper right image of Figure 5c indicate the appearance of particles adsorbed on regions of the GDE that were not covered by the Ag-NC catalyst material prior to CO<sub>2</sub>RR. This phenomenon was more evident on cathodes subjected to 32 min ( $1600 \text{ C cm}^{-2}$ ) of electrolysis. Figure 5d demonstrates that the particles formed near the Ag-NCs when treated with these longer reaction times increased not only in size ( $\sim 10 \text{ nm}$ ) but also in population along the formerly catalyst-free substrate regions. This is also supported by the EDX mapping shown in Figure 5e acquired on the sample location highlighted by the blue rectangle in Figure 5d. Additionally, analysis of single Ag-NCs indicated that the material source for these electrochemically formed particles stems mainly from the cube's vertices, eventually leading to the appearance of

small (111) planes of truncated cube-like particles (Figure S3). Thus, it is clear that monitoring of the electrochemically induced morphological evolution of the colloidal catalyst is accurately described provided that the nanoparticles are not passivated by electron beam irradiation prior to electrolysis (as is the case in IL-SEM investigations). We suggest, however, that the observed mild morphological alteration of the Ag-NC catalyst on the GDE surfaces alone cannot be the physical origin for the significantly affected  $\text{PCD}_{\text{CO}}$ s and  $\text{FE}_{\text{CO}}$ s, as shown in Figure 3 panels d and f, at potentials more negative than  $-1.8 \text{ V}$ .

To elucidate whether this decay in performance originates instead from the high bulk pH value ( $\sim 14$ ) of the electrolyte used, reference CO<sub>2</sub>RR electrochemical and SEM experiments similar to those shown in Figures 3 and 5 were carried out on Ag-NC-GDEs, employing a significantly less basic 2 M KHCO<sub>3</sub> electrolyte ( $\text{pH} \sim 8$ ). These results are displayed in Figures S4 and S5 following the same color code and image representation as of Figures 3 and 5. Figure S4a,b shows the corresponding FEs and PCDs of the electrogenerated gaseous products. Besides a slightly lower  $\text{PCD}_{\text{CO}}$  at most cathodic applied potentials ( $-1.86 \text{ V} \geq E \geq -2.14 \text{ V}$ ), all other displayed quantities ( $\text{PCD}_{\text{H}_2}$ ,  $\text{FE}_{\text{CO}}$ , and  $\text{FE}_{\text{H}_2}$ ) exhibited the same qualitative potential- and time-dependent behaviors after 10 min CO<sub>2</sub> electrolysis, as discussed above, when the 2 M KOH electrolyte was used (compare Figure 3c–f with Figure S4c–f). The reduction in  $\text{PCD}_{\text{CO}}$  at high applied potentials might be related to the lower ionic conductivity of the HCO<sub>3</sub><sup>−</sup> ion in comparison to that of OH<sup>−</sup> and its relative deficiency to lower the CO<sub>2</sub> activation energy barrier.<sup>42</sup> Interestingly, suppression of the parasitic HER was equally effective when using both supporting electrolytes. The fact that the temporal dependence of  $\text{FE}_{\text{CO}}$  and  $\text{PCD}_{\text{CO}}$  as the electrolysis proceeded revealed again a stability bifurcation that depended on the potential window examined (Figure S4c–f) but not on the specific bulk pH is not surprising. Indeed, it has been predicted that the local pH adjacent to the three-phase boundary layer of

a gas-fed GDE at CO<sub>2</sub>RR reaction rates above 50 mA cm<sup>-2</sup> becomes rather similar for both neutral and highly alkaline electrolytes due to the driven cathode half reactions (both CO<sub>2</sub> and water reduction generate OH<sup>-</sup> as a byproduct).<sup>30</sup> The difference in the local pH at the cathode between both electrolyte solutions under CO<sub>2</sub>RR reacting conditions at targeted  $j_s \geq 200$  mA cm<sup>-2</sup> might actually be negligible.<sup>30</sup> Similar to the experiments conducted in the 2 M KOH electrolyte, as shown in Figure 5, SEM analysis of a Ag-NC-GDE after 60 min CO<sub>2</sub>RR at mild applied potential ( $E = -1.84$  V, 1600 C cm<sup>-2</sup>) in 2 M KHCO<sub>3</sub> showed minor structural degradation of the Ag-NCs (Figure S5). This finding suggests that the performance decay in our gas-fed zero-gap flow cell at large CO<sub>2</sub>RR rates might be more significantly influenced by the increased local alkalinity rather than the relatively minor structural degradation of the Ag-NCs and the original bulk pH. Furthermore, an increasingly high alkalinity at the three-boundary layer in GDEs has been found to lead to issues related to electrolyte carbonation, electrolyte penetration through the GDE body (electrode flooding), and salt precipitation.<sup>39,43,44,49,51</sup> Electrolyte intrusion beyond the MPL of the Ag-NC-GDEs at high cathodic potentials also contributes to the decay in FE<sub>CO</sub> and PCD<sub>CO</sub>, as observed in Figure 3d,f and S4d,f, due to an increase of the CO<sub>2</sub> diffusion length. This is in agreement with recently reported work by Leonard et al.<sup>43</sup> who observed a clear increase of flooding propensity and loss of the nominal MPL hydrophobicity under stringent CO<sub>2</sub>RR reductive conditions.

To further support this argument, we resorted to investigations performed in conventional H-cell configurations in which none of these detrimental aspects would influence the supply of dissolved CO<sub>2</sub> to the cathode through the liquid electrolyte. Figure 6a,b summarizes these experimental results. In comparison to the gas-fed experiments, significantly lower PCD<sub>CO</sub>s are observed in all of the inspected potential window due to the dominant effect of the mass transport limitations of CO<sub>2</sub> dissolved in the used 2 M KHCO<sub>3</sub> electrolyte. In addition, the use of this non-optimal,<sup>9,21-24</sup> almost neutral electrolyte leads to larger PCD<sub>H<sub>2</sub>S</sub> (as great as PCD<sub>H<sub>2</sub></sub> ~ 100 mA cm<sup>-2</sup>) at high cathodic potentials relative to the values observed in the zero-gap experiments. The potential-dependent product selectivity shows an increase of FE<sub>CO</sub> as the potential varied from low to mild applied values ( $-1.4$  V  $\geq E \geq -1.6$  V), although in contrast to the observed trends for the more technical approach, the CO efficiency significantly decreases as the competing HER benefits at more negative values. Moreover, in contrast to the results from the zero-gap experiments, neither FE<sub>CO</sub> nor PCD<sub>CO</sub> decays from its initial value as the electrolysis reaction proceeds, regardless of the applied potential (Figure 6c,d). Considering that the Ag-NCs used in these H-cell experiments seem to have undergone a similar degree of degradation and associated mechanism at mild and high applied potentials relative to that of the zero-gap counterparts (Figures 6e-f and S6), it seems evident that the system stability issues acting at high potentials and longer electrolysis times in the gas-fed configuration stem mainly from a sub-optimal reactor design and the high local alkalinity at high current densities. Indeed, we found a clear correlation between the decaying FE<sub>CO</sub> and PCD<sub>CO</sub> and occurrence of GDE flooding and salt precipitation, which cause device performance failure at high cathodic potentials in the gas-fed approach. Figure S7a,b shows typical contact angle images for

water droplets on Ag-NC-GDEs before and after being submitted to CO<sub>2</sub>RR at  $-2.07$  V for 32 min. The decrease of contact angle indicates that the barrier properties of the MPL are to some extent undermined upon electrolysis. The corresponding EDX spectra additionally show a clear decay of the F signal due to degradation of the hydrophobic PTFE coating of the MPL (Figure S7c). Moreover, Figure S8a presents optical images showing the typical appearance of the employed GDEs at different experimental stages (as-received GDE, as-prepared Ag-NC-GDE and Ag-NC-GDE after having sustained CO<sub>2</sub>RR at  $-2.07$  V for 32 min and 1600 C cm<sup>-2</sup>). The EDX spectra and mapping displayed in Figure S8b,c further support that, under these drastic cathodic conditions, carbonate/bicarbonate precipitation on the catalyst-modified GDE surface and its periphery takes place. Additionally, Figures S9 and S10 show that these undesired events (flooding and precipitation) can even be observed on the backside of such electrodes, irrespectively of the employed electrolyte. We would like to emphasize that this kind of massive salt precipitation is only observed in the GDE approach, irrespectively of the used electrolyte, but not in the H-type cell configuration where the partial current densities of CO formation are mass transport limited and remain stable during electrolysis.

**Comparison of CO<sub>2</sub>RR Product Distribution in Zero-Gap Flow Cell and H-Type Cell.** Finally, another important aspect that requires attention is the spectrum of products yielded from CO<sub>2</sub>RR processes, which might also be affected by the specificities of the experimental approach employed (cell design and environment).<sup>62</sup> Along these lines, fundamental differences regarding the product selectivity were observed between the gas-fed- and H-cell-based approaches. As illustrated in Figure S11, formate was detected as a CO<sub>2</sub> electrolysis product over a large potential window using alkaline as well as almost basic electrolytes when the zero-gap testbed was used. This finding is in agreement with reports by Sargent, Sinton et al. on increased formate production on Ag-GDEs in highly alkaline aqueous environments (Figure 1a).<sup>40</sup> These authors proposed that the enhanced formate production when using highly alkaline environments adjacent to the Ag-GDE might be due to the limited ability of a temporary H<sub>3</sub>O<sup>+</sup> molecule that is believed to assist the first protonation step of the adsorbed \*COOH intermediate on the CO reaction pathway.<sup>63</sup> Accordingly, Figure S11 shows that both FE<sub>HCOO<sup>-</sup></sub> and PCD<sub>HCOO<sup>-</sup></sub> were more prominent when the hydroxide-based solution was employed and peaked at  $E \sim -1.87$  V, amounting to non-negligible values of FE<sub>HCOO<sup>-</sup></sub> ~ 20.1% and PCD<sub>HCOO<sup>-</sup></sub> ~ 148 mA cm<sup>-2</sup>, respectively. This result agrees with a recent report by Seger et al. who identified formate as a significant CO<sub>2</sub>RR side reaction using a zero-gap electrolyzer combined with a basic anolyte at high current densities  $\geq 200$  mA cm<sup>-2</sup>.<sup>46</sup> Conversely, our experiments in the H-cell yielded only a minor formate contribution at the highest applied potential (FE<sub>HCOO<sup>-</sup></sub> ~ 2.6% and PCD<sub>HCOO<sup>-</sup></sub> ~ 7.5 mA cm<sup>-2</sup>). This result underlines the fact that the vast knowledge developed through batch-type CO<sub>2</sub>RR experiments does not necessarily translate to more practical approaches aimed at industrial CO<sub>2</sub> reduction. Therefore, more effort must be devoted to understanding the particularities inherent to gas-fed CO<sub>2</sub>RR platforms by going beyond a purely catalyst development-oriented approach and focusing more on rational electrolyzer design, engineering solutions, and process optimization to provide more robust and stable gas-liquid

interfaces. Precipitation and flooding phenomena might, for instance, be prevented through incorporation of application-tailored microstructures and wettability into novel GDE designs.<sup>43</sup> Encouraging efforts in this direction are being made, for instance, by Schmid et al.<sup>64</sup> who have recently addressed the importance of optimized operating modes, electrolyzer design, and materials selection that enable nearly practical scale electrochemical CO<sub>2</sub>-to-CO conversion. One key finding of these investigations that enables stable and long-term CO<sub>2</sub>RR operation at  $-200 \text{ mA cm}^{-2}$  is the attenuation of salt precipitation, GDE flooding, and CO<sub>2</sub> crossover to the anode compartment by utilizing a carbonate-free, sulfate-based neutral electrolyte in a liquid flow-cell electrolyzer.

## CONCLUSIONS

We studied the performance of a model Ag–NC catalyst for CO<sub>2</sub>RR to carbon monoxide on technical GDE in a zero-gap configuration and highly alkaline environments. The system exhibited remarkable CO<sub>2</sub> to CO conversion figures in terms of FE and PCD (FE<sub>CO</sub>  $\sim 625 \text{ mA cm}^{-2}$  and PCD<sub>CO</sub>  $\sim 85\%$ ) even at sub-monolayer Ag–NC catalyst coverages on the GDEs. Based on the temporal system stability that they promoted, two apparent potential regimes were identified for FE<sub>CO</sub> and PCD<sub>CO</sub>. At mild applied potentials ( $-1.5 \text{ V} > E$  vs Ag/AgCl  $> -1.8 \text{ V}$ ), the CO<sub>2</sub>RR process improved or remained stable over time reaching PCD<sub>CO</sub>  $> 300 \text{ mA cm}^{-2}$  and FE  $\sim 85\%$ . However, at greater cathodic potentials, both CO production figures were initially more prominent but then weakened over time. This decline was initially mild but intensified abruptly after  $\sim 30 \text{ min}$  with increasing applied potential. The morphological evolution of the Ag–NCs on the GDEs induced by the CO<sub>2</sub>RR as well as the direct mechanical contact between the catalyst layer and anion-exchange membrane was analyzed by IL–SEM and post-electrolysis SEM investigations. The former approach turned out to be unsuitable for structural characterization of electrolysis-induced changes on colloidal catalysts that bear a surfactant shell on their surface left behind from the synthesis method. On the other hand, post-electrolysis SEM studies enabled the true morphological evolution of the catalyst that strongly depended on the applied electrolysis conditions. Regardless of the applied experimental conditions, no detachment of Ag–NC particles from the GDEs was detected. It was found that at low and mild potentials, the Ag–NCs undergo insignificant morphological alteration. However, at harsher cathodic conditions, smaller Ag nanoparticles begin to appear, adsorbed on formerly catalyst-free substrate regions. The material source of these electrochemically generated nanoparticles seems to come from the corners of the Ag–NCs. The observed mild cathodic corrosion of the catalyst leads to slightly truncated cube morphologies. However, complementary CO<sub>2</sub>RR experiments in a neutral environment on Ag–NC–GDEs conducted in both zero-gap and conventional H-type cell configurations suggest that system failure is rooted in more factors than the observed morphological degradation of the catalyst. That is, the high alkalinity level at the three-phase boundary layer where the fed CO<sub>2</sub>, catalyst material, and polymer electrolyte meet leads, to a significant degree, to the observed CO<sub>2</sub>RR performance decline. The high alkalinity level inevitably develops at the reaction interface in the zero-gap electrolyzers at high cathodic reaction rates  $>300 \text{ mA cm}^{-2}$  even when the starting bulk electrolyte is neutral, thereby causing electrolyte percolation through the GDEs, electrode flooding, and salt

precipitation. Thus, this work enables the deconvolution of catalyst structural stability from system performance stability. Although the application of higher catalyst loadings on the GDEs would probably alleviate these issues, a more robust, long-lasting solution to the intrinsic challenges posed by gas-fed approaches must be proposed to near industrial CO<sub>2</sub>RR deployment. Finally, as stated by some other recent works, we suggest that CO<sub>2</sub>RR studies should increasingly be performed using technical approaches because the conclusions extracted from H-type cell experiments might not be directly translatable to electrolyzer-based studies.

## ASSOCIATED CONTENT

### Supporting Information

The Supporting Information is available free of charge at <https://pubs.acs.org/doi/10.1021/acscatal.0c03609>.

SEM, EDX, XRD, and edge size distribution of Ag–NCs; literature survey on CO<sub>2</sub>RR to CO on Ag–GDEs; IL–SEM of Ag–NC–GDEs subjected to zero-gap CO<sub>2</sub>RR in 2 M KOH; SEM image of single Ag–NCs after zero-gap CO<sub>2</sub>RR in 2 M KOH at high cathodic potentials; potential-dependent FEs and PCDs from zero-gap CO<sub>2</sub>RR in 2 M KHCO<sub>3</sub>; SEM imaging of Ag–NCs–GDEs after zero-gap CO<sub>2</sub>RR in 2 M KHCO<sub>3</sub>; SEM imaging of Ag–NCs–GDEs after CO<sub>2</sub>RR in H-type cell; optical micrographs of employed GDEs at different experimental stages and EDX characterization of a Ag–NC–GDE after CO<sub>2</sub>RR in 2 M KOH at stringent cathodic conditions; potential-dependent FE<sub>HCOO<sup>-</sup></sub> and PCD<sub>HCOO<sup>-</sup></sub> from zero-gap CO<sub>2</sub>RR in 2 M KOH and 2 M KHCO<sub>3</sub>; and complete database of all experiments (PDF)

## AUTHOR INFORMATION

### Corresponding Authors

**Pavel Moreno-García** – Department of Chemistry and Biochemistry, University of Bern, Bern 3012, Switzerland; [orcid.org/0000-0002-6827-787X](https://orcid.org/0000-0002-6827-787X); Email: [pavel.moreno@dcb.unibe.ch](mailto:pavel.moreno@dcb.unibe.ch)

**Peter Broekmann** – Department of Chemistry and Biochemistry, University of Bern, Bern 3012, Switzerland; [orcid.org/0000-0002-6287-1042](https://orcid.org/0000-0002-6287-1042); Email: [peter.broekmann@dcb.unibe.ch](mailto:peter.broekmann@dcb.unibe.ch)

### Authors

**María de Jesus Gálvez-Vázquez** – Department of Chemistry and Biochemistry, University of Bern, Bern 3012, Switzerland

**Heng Xu** – Department of Chemistry, Duke University, Durham, North Carolina 27708-0354, United States

**Yuhui Hou** – Department of Chemistry and Biochemistry, University of Bern, Bern 3012, Switzerland; [orcid.org/0000-0003-1616-562X](https://orcid.org/0000-0003-1616-562X)

**Huifang Hu** – Department of Chemistry and Biochemistry, University of Bern, Bern 3012, Switzerland

**Iván Zelocualtecatl Montiel** – Department of Chemistry and Biochemistry, University of Bern, Bern 3012, Switzerland

**Alexander V. Rudnev** – Department of Chemistry and Biochemistry, University of Bern, Bern 3012, Switzerland; A.N. Frumkin Institute of Physical Chemistry and Electrochemistry Russian Academy of Sciences, Moscow 119071, Russia

**Shima Alinejad** – Department of Chemistry and Biochemistry, University of Bern, Bern 3012, Switzerland; [orcid.org/0000-0002-1151-3333](https://orcid.org/0000-0002-1151-3333)

**Vitali Grozovski** – Department of Chemistry and Biochemistry, University of Bern, Bern 3012, Switzerland

**Benjamin J. Wiley** – Department of Chemistry, Duke University, Durham, North Carolina 27708-0354, United States; [orcid.org/0000-0002-1314-6223](https://orcid.org/0000-0002-1314-6223)

**Matthias Arenz** – Department of Chemistry and Biochemistry, University of Bern, Bern 3012, Switzerland; [orcid.org/0000-0001-9765-4315](https://orcid.org/0000-0001-9765-4315)

Complete contact information is available at:  
<https://pubs.acs.org/10.1021/acscatal.0c03609>

### Author Contributions

<sup>†</sup>M.J.G.-V. and P.M.G. contributed equally. The manuscript was written through contributions of all authors. All authors have given approval to the final version of the manuscript.

### Notes

The authors declare no competing financial interest.

### ACKNOWLEDGMENTS

Support by the CTI Swiss Competence Center for Energy Research (SCCER Heat and Electricity Storage) is gratefully acknowledged. P.B. acknowledges financial support from the Swiss National Foundation (grant 200020-172507). M.d.J.G.-V. acknowledges the financial support by the Swiss Government Excellence Scholarships for Foreign Scholars (ESKAS) and thanks Antonio Calderon I. for the preparation of the cell's schematic drawings. A. R. acknowledges financial support from the Ministry of Science and Higher Education of the Russian Federation. M.A. acknowledges funding from the Swiss National Science Foundation (SNSF) via the project No. 200021\_184742.

### REFERENCES

- (1) Vennekoetter, J.-B.; Sengpiel, R.; Wessling, M. Beyond the catalyst: How electrode and reactor design determine the product spectrum during electrochemical CO<sub>2</sub> reduction. *Chem. Eng. J.* **2019**, *364*, 89–101.
- (2) Wang, Y.; Xia, Q.; Bai, X.; Ge, Z.; Yang, Q.; Yin, C.; Kang, S.; Dong, M.; Li, X. Carbothermal activation synthesis of 3D porous g-C<sub>3</sub>N<sub>4</sub>/carbon nanosheets composite with superior performance for CO<sub>2</sub> photoreduction. *Appl. Catal., B* **2018**, *239*, 196–203.
- (3) Jhong, H.-R. M.; Ma, S.; Kenis, P. J. Electrochemical conversion of CO<sub>2</sub> to useful chemicals: current status, remaining challenges, and future opportunities. *Curr. Opin. Chem. Eng.* **2013**, *2*, 191–199.
- (4) Seh, Z. W.; Kibsgaard, J.; Dickens, C. F.; Chorkendorff, I.; Nørskov, J. K.; Jaramillo, T. F. Combining theory and experiment in electrocatalysis: Insights into materials design. *Science* **2017**, *355*, No. eaad4998.
- (5) Kibria, M. G.; Edwards, J. P.; Gabardo, C. M.; Dinh, C. T.; Seifitokaldani, A.; Sinton, D.; Sargent, E. H. Electrochemical CO<sub>2</sub> Reduction into Chemical Feedstocks: From Mechanistic Electrocatalysis Models to System Design. *Adv. Mater.* **2019**, *31*, 1807166.
- (6) Fan, M.; Prabhudev, S.; Garbarino, S.; Qiao, J.; Botton, G. A.; Harrington, D. A.; Tavares, A. C.; Guay, D. Uncovering the Nature of Electroactive Sites in Nano Architected Dendritic Bi for Highly Efficient CO<sub>2</sub> Electroreduction to Formate. *Appl. Catal., B* **2020**, *274*, 119031.
- (7) Hori, Y. *Electrochemical CO<sub>2</sub> Reduction on Metal Electrodes in Modern Aspects of Electrochemistry*; Springer: NY, 2008; p 89–189.
- (8) Bushuyev, O. S.; De Luna, P.; Dinh, C. T.; Tao, L.; Saur, G.; van de Lagemaat, J.; Kelley, S. O.; Sargent, E. H. What Should We Make with CO<sub>2</sub> and How Can We Make It? *Joule* **2018**, *2*, 825–832.

(9) Jouny, M.; Luc, W.; Jiao, F. High-rate electroreduction of carbon monoxide to multi-carbon products. *Nat. Catal.* **2018**, *1*, 748–755.

(10) Haas, T.; Krause, R.; Weber, R.; Demler, M.; Schmid, G. Technical photosynthesis involving CO<sub>2</sub> electrolysis and fermentation. *Nat. Catal.* **2018**, *1*, 32–39.

(11) Ma, S.; Liu, J.; Sasaki, K.; Lyth, S. M.; Kenis, P. J. A. Carbon Foam Decorated with Silver Nanoparticles for Electrochemical CO<sub>2</sub> Conversion. *Energy Technol.* **2017**, *5*, 861–863.

(12) Dutta, A.; Morstein, C. E.; Rahaman, M.; Cedeño López, A.; Broekmann, P. Beyond Copper in CO<sub>2</sub> Electrolysis: Effective Hydrocarbon Production on Silver-Nanofoam Catalysts. *ACS Catal.* **2018**, *8*, 8357–8368.

(13) Hatsukade, T.; Kuhl, K. P.; Cave, E. R.; Abram, D. N.; Jaramillo, T. F. Insights into the electrocatalytic reduction of CO<sub>2</sub> on metallic silver surfaces. *Phys. Chem. Chem. Phys.* **2014**, *16*, 13814–13819.

(14) Chen, Y.; Li, C. W.; Kanan, M. W. Aqueous CO<sub>2</sub> Reduction at Very Low Overpotential on Oxide-Derived Au Nanoparticles. *J. Am. Chem. Soc.* **2012**, *134*, 19969–19972.

(15) Nursanto, E. B.; Jeon, H. S.; Kim, C.; Jee, M. S.; Koh, J. H.; Hwang, Y. J.; Min, B. K. Gold catalyst reactivity for CO<sub>2</sub> electroreduction: From nano particle to layer. *Catal. Today* **2016**, *260*, 107–111.

(16) Won, D. H.; Shin, H.; Koh, J.; Chung, J.; Lee, H. S.; Kim, H.; Woo, S. I. Highly Efficient, Selective, and Stable CO<sub>2</sub> Electroreduction on a Hexagonal Zn Catalyst. *Angew. Chem., Int. Ed.* **2016**, *55*, 9297–9300.

(17) Moreno-García, P.; Schlegel, N.; Zanetti, A.; Cedeño López, A.; Gálvez-Vázquez, M. d. J.; Dutta, A.; Rahaman, M.; Broekmann, P. Selective Electrochemical Reduction of CO<sub>2</sub> to CO on Zn-Based Foams Produced by Cu<sup>2+</sup> and Template-Assisted Electrodeposition. *ACS Appl. Mater. Interfaces* **2018**, *10*, 31355–31365.

(18) Luo, W.; Zhang, Q.; Zhang, J.; Moili, E.; Zhao, K.; Züttel, A. Electrochemical reconstruction of ZnO for selective reduction of CO<sub>2</sub> to CO. *Appl. Catal., B* **2020**, *273*, 119060.

(19) Yang, M.; Zhang, J.; Cao, Y.; Wu, M.; Qian, K.; Zhang, Z.; Liu, H.; Wang, J.; Chen, W.; Huang, W. Facet Sensitivity of Capping Ligand-Free Ag Crystals in CO<sub>2</sub> Electrochemical Reduction to CO. *ChemCatChem* **2018**, *10*, 5128–5134.

(20) Liu, S.; Tao, H.; Zeng, L.; Liu, Q.; Xu, Z.; Liu, Q.; Luo, J.-L. Shape-Dependent Electrocatalytic Reduction of CO<sub>2</sub> to CO on Triangular Silver Nanoplates. *J. Am. Chem. Soc.* **2017**, *139*, 2160–2163.

(21) Dinh, C.-T.; Burdyny, T.; Kibria, M. G.; Seifitokaldani, A.; Gabardo, C. M.; García de Arquer, F. P.; Kiani, A.; Edwards, J. P.; De Luna, P.; Bushuyev, O. S.; Zou, C.; Quintero-Bermudez, R.; Pang, Y.; Sinton, D.; Sargent, E. H. CO<sub>2</sub> electroreduction to ethylene via hydroxide-mediated copper catalysis at an abrupt interface. *Science* **2018**, *360*, 783–787.

(22) Hoang, T. T. H.; Verma, S.; Ma, S.; Fister, T. T.; Timoshenko, J.; Frenkel, A. I.; Kenis, P. J. A.; Gewirth, A. A. Nanoporous Copper–Silver Alloys by Additive-Controlled Electrodeposition for the Selective Electroreduction of CO<sub>2</sub> to Ethylene and Ethanol. *J. Am. Chem. Soc.* **2018**, *140*, 5791–5797.

(23) Kim, B.; Hillman, F.; Ariyoshi, M.; Fujikawa, S.; Kenis, P. J. A. Effects of composition of the micro porous layer and the substrate on performance in the electrochemical reduction of CO<sub>2</sub> to CO. *J. Power Sources* **2016**, *312*, 192–198.

(24) Liu, M.; Pang, Y.; Zhang, B.; De Luna, P.; Voznyy, O.; Xu, J.; Zheng, X.; Dinh, C. T.; Fan, F.; Cao, C.; de Arquer, F. P. G.; Safaei, T. S.; Mepham, A.; Klinkova, A.; Kumacheva, E.; Filleter, T.; Sinton, D.; Kelley, S. O.; Sargent, E. H. Enhanced electrocatalytic CO<sub>2</sub> reduction via field-induced reagent concentration. *Nature* **2016**, *537*, 382–386.

(25) Liu, Z.; Yang, H.; Kutz, R.; Masel, R. I. CO<sub>2</sub> Electrolysis to CO and O<sub>2</sub> at High Selectivity, Stability and Efficiency Using Sustainion Membranes. *J. Electrochem. Soc.* **2018**, *165*, J3371–J3377.

(26) Kas, R.; Hummadi, K. K.; Kortlever, R.; de Wit, P.; Milbrat, A.; Luiten-Olieman, M. W. J.; Benes, N. E.; Koper, M. T. M.; Mul, G. Three-dimensional porous hollow fibre copper electrodes for efficient

and high-rate electrochemical carbon dioxide reduction. *Nat. Commun.* **2016**, *7*, 10748.

(27) Ma, S.; Sadakiyo, M.; Luo, R.; Heima, M.; Yamauchi, M.; Kenis, P. J. A. One-step electrosynthesis of ethylene and ethanol from CO<sub>2</sub> in an alkaline electrolyzer. *J. Power Sources* **2016**, *301*, 219–228.

(28) Moreno-García, P.; Kovács, N.; Grozovski, V.; Gálvez-Vázquez, M. d. J.; Vesztergom, S.; Broekmann, P. Toward CO<sub>2</sub> Electroreduction under Controlled Mass Flow Conditions: A Combined Inverted RDE and Gas Chromatography Approach. *Anal. Chem.* **2020**, *92*, 4301–4308.

(29) Kim, C.; Dionigi, F.; Beermann, V.; Wang, X.; Möller, T.; Strasser, P. Alloy Nanocatalysts for the Electrochemical Oxygen Reduction (ORR) and the Direct Electrochemical Carbon Dioxide Reduction Reaction (CO<sub>2</sub>RR). *Adv. Mater.* **2019**, *31*, 1805617.

(30) Burdyny, T.; Smith, W. A. CO<sub>2</sub> reduction on gas-diffusion electrodes and why catalytic performance must be assessed at commercially-relevant conditions. *Energy Environ. Sci.* **2019**, *12*, 1442–1453.

(31) De Gregorio, G. L.; Burdyny, T.; Loiudice, A.; Iyengar, P.; Smith, W. A.; Buonsanti, R. Facet-dependent selectivity of Cu catalysts in electrochemical CO<sub>2</sub> reduction at commercially viable current densities. *ACS Catal.* **2020**, *10*, 4854–4862.

(32) Delacourt, C.; Ridgway, P. L.; Kerr, J. B.; Newman, J. Design of an Electrochemical Cell Making Syngas (CO+H<sub>2</sub>) from CO<sub>2</sub> and H<sub>2</sub> Reduction at Room Temperature. *J. Electrochem. Soc.* **2008**, *155*, B42.

(33) Dufek, E. J.; Lister, T. E.; McIlwain, M. E. Bench-scale electrochemical system for generation of CO and syn-gas. *J. Appl. Electrochem.* **2011**, *41*, 623–631.

(34) Higgins, D.; Hahn, C.; Xiang, C.; Jaramillo, T. F.; Weber, A. Z. Gas-Diffusion Electrodes for Carbon Dioxide Reduction: A New Paradigm. *ACS Energy Lett.* **2019**, *4*, 317–324.

(35) Weekes, D. M.; Salvatore, D. A.; Reyes, A.; Huang, A.; Berlinguette, C. P. Electrolytic CO<sub>2</sub> Reduction in a Flow Cell. *Acc. Chem. Res.* **2018**, *51*, 910–918.

(36) Gálvez-Vázquez, M. d. J.; Alinejad, S.; Hu, H.; Hou, Y.; Moreno-García, P.; Zana, A.; Wiberg, G. K. H.; Broekmann, P.; Arenz, M. Testing a Silver Nanowire Catalyst for the Selective CO<sub>2</sub> Reduction in a Gas Diffusion Electrode Half-cell Setup Enabling High Mass Transport Conditions. *Chimia* **2019**, *73*, 922–927.

(37) Verma, S.; Lu, X.; Ma, S.; Masel, R. I.; Kenis, P. J. A. The effect of electrolyte composition on the electroreduction of CO<sub>2</sub> to CO on Ag based gas diffusion electrodes. *Phys. Chem. Chem. Phys.* **2016**, *18*, 7075–7084.

(38) Verma, S.; Hamasaki, Y.; Kim, C.; Huang, W.; Lu, S.; Jhong, H.-R. M.; Gewirth, A. A.; Fujigaya, T.; Nakashima, N.; Kenis, P. J. A. Insights into the Low Overpotential Electroreduction of CO<sub>2</sub> to CO on a Supported Gold Catalyst in an Alkaline Flow Electrolyzer. *ACS Energy Lett.* **2018**, *3*, 193–198.

(39) Dinh, C.-T.; Garcia de Arquer, F. P.; Sinton, D.; Sargent, E. H. High Rate, Selective, and Stable Electroreduction of CO<sub>2</sub> to CO in Basic and Neutral Media. *ACS Energy Lett.* **2018**, *3*, 2835–2840.

(40) Gabardo, C. M.; Seifitokaldani, A.; Edwards, J. P.; Dinh, C.-T.; Burdyny, T.; Kibria, M. G.; O'Brien, C. P.; Sargent, E. H.; Sinton, D. Combined high alkalinity and pressurization enable efficient CO<sub>2</sub> electroreduction to CO. *Energy Environ. Sci.* **2018**, *11*, 2531–2539.

(41) Dufek, E. J.; Lister, T. E.; McIlwain, M. E. Influence of Electrolytes and Membranes on Cell Operation for Syn-Gas Production. *Electrochem. Solid-State Lett.* **2012**, *15*, B48.

(42) Bhargava, S. S.; Proietto, F.; Azmoodeh, D.; Cofell, E. R.; Henckel, D. A.; Verma, S.; Brooks, C. J.; Gewirth, A. A.; Kenis, P. J. A. System Design Rules for Intensifying the Electrochemical Reduction of CO<sub>2</sub> to CO on Ag Nanoparticles. *ChemElectroChem* **2020**, *7*, 2001–2011.

(43) Leonard, M. E.; Clarke, L. E.; Forner-Cuenca, A.; Brown, S. M.; Brushett, F. R. Investigating Electrode Flooding in a Flowing Electrolyte, Gas-Fed Carbon Dioxide Electrolyzer. *ChemSusChem* **2020**, *13*, 400–411.

(44) Pătru, A.; Binninger, T.; Příbyl, B.; Schmidt, T. J. Design Principles of Bipolar Electrochemical Co-Electrolysis Cells for

Efficient Reduction of Carbon Dioxide from Gas Phase at Low Temperature. *J. Electrochem. Soc.* **2019**, *166*, F34–F43.

(45) Ma, M.; Clark, E. L.; Therkildsen, K. T.; Dalsgaard, S.; Chorkendorff, I.; Seger, B. Insights into the carbon balance for CO<sub>2</sub> electroreduction on Cu using gas diffusion electrode reactor designs. *Energy Environ. Sci.* **2020**, *13*, 977–985.

(46) Larrazábal, G. O.; Strøm-Hansen, P.; Heli, J. P.; Zeiter, K.; Therkildsen, K. T.; Chorkendorff, I.; Seger, B. Analysis of Mass Flows and Membrane Cross-over in CO<sub>2</sub> Reduction at High Current Densities in an MEA-Type Electrolyzer. *ACS Appl. Mater. Interfaces* **2019**, *11*, 41281–41288.

(47) Liu, Z.; Masel, R. I.; Chen, Q.; Kutz, R.; Yang, H.; Lewinski, K.; Kaplun, M.; Luopa, S.; Lutz, D. R. Electrochemical generation of syngas from water and carbon dioxide at industrially important rates. *J. CO<sub>2</sub> Util.* **2016**, *15*, 50–56.

(48) Kutz, R. B.; Chen, Q.; Yang, H.; Sajjad, S. D.; Liu, Z.; Masel, R. I. R. Sustainion Imidazolium-Functionalized Polymers for Carbon Dioxide Electrolysis. *Energy Technol.* **2017**, *5*, 929–936.

(49) Weng, L.-C.; Bell, A. T.; Weber, A. Z. Towards membrane-electrode assembly systems for CO<sub>2</sub> reduction: a modeling study. *Energy Environ. Sci.* **2019**, *12*, 1950–1968.

(50) Yin, Z.; Peng, H.; Wei, X.; Zhou, H.; Gong, J.; Huai, M.; Xiao, L.; Wang, G.; Lu, J.; Zhuang, L. An alkaline polymer electrolyte CO<sub>2</sub> electrolyzer operated with pure water. *Energy Environ. Sci.* **2019**, *12*, 2455–2462.

(51) Jeanty, P.; Scherer, C.; Magori, E.; Wiesner-Fleischer, K.; Hinrichsen, O.; Fleischer, M. Upscaling and continuous operation of electrochemical CO<sub>2</sub> to CO conversion in aqueous solutions on silver gas diffusion electrodes. *J. CO<sub>2</sub> Util.* **2018**, *24*, 454–462.

(52) Wiley, B.; Sun, Y.; Xia, Y. Polyol Synthesis of Silver Nanostructures: Control of Product Morphology with Fe(II) or Fe(III) Species. *Langmuir* **2005**, *21*, 8077–8080.

(53) Skrabalak, S. E.; Au, L.; Li, X.; Xia, Y. Facile synthesis of Ag nanocubes and Au nanocages. *Nat. Protoc.* **2007**, *2*, 2182–2190.

(54) Li, Y. C.; Zhou, D.; Yan, Z.; Gonçalves, R. H.; Salvatore, D. A.; Berlinguette, C. P.; Mallouk, T. E. Electrolysis of CO<sub>2</sub> to Syngas in Bipolar Membrane-Based Electrochemical Cells. *ACS Energy Lett.* **2016**, *1*, 1149–1153.

(55) Salvatore, D. A.; Weekes, D. M.; He, J.; Dettelbach, K. E.; Li, Y. C.; Mallouk, T. E.; Berlinguette, C. P. Electrolysis of Gaseous CO<sub>2</sub> to CO in a Flow Cell with a Bipolar Membrane. *ACS Energy Lett.* **2018**, *3*, 149–154.

(56) Mayrhofer, K. J. J.; Meier, J. C.; Ashton, S. J.; Wiberg, G. K. H.; Kraus, F.; Hanzlik, M.; Arenz, M. Fuel cell catalyst degradation on the nanoscale. *Electrochem. Commun.* **2008**, *10*, 1144–1147.

(57) Hodnik, N.; Zorko, M.; Bele, M.; Hočevar, S.; Gabersček, M. Identical Location Scanning Electron Microscopy: A Case Study of Electrochemical Degradation of PtNi Nanoparticles Using a New Nondestructive Method. *J. Phys. Chem. C* **2012**, *116*, 21326–21333.

(58) Rahaman, M.; Dutta, A.; Zanetti, A.; Broekmann, P. Electrochemical Reduction of CO<sub>2</sub> into Multicarbon Alcohols on Activated Cu Mesh Catalysts: An Identical Location (IL) Study. *ACS Catal.* **2017**, *7*, 7946–7956.

(59) Luo, B.; Fang, Y.; Li, J.; Huang, Z.; Hu, B.; Zhou, J. Improved Stability of Metal Nanowires via Electron Beam Irradiation Induced Surface Passivation. *ACS Appl. Mater. Interfaces* **2019**, *11*, 12195–12201.

(60) Tan, S. F.; Bosman, M.; Nijhuis, C. A. Molecular Coatings for Stabilizing Silver and Gold Nanocubes under Electron Beam Irradiation. *Langmuir* **2017**, *33*, 1189–1196.

(61) Huang, J.; Hörmann, N.; Oveisi, E.; Loiudice, A.; De Gregorio, G. L.; Andreussi, O.; Marzari, N.; Buonsanti, R. Potential-induced nanoclustering of metallic catalysts during electrochemical CO<sub>2</sub> reduction. *Nat. Commun.* **2018**, *9*, 3117.

(62) Wang, G.; Pan, J.; Jiang, S. P.; Yang, H. Gas phase electrochemical conversion of humidified CO<sub>2</sub> to CO and H<sub>2</sub> on proton-exchange and alkaline anion-exchange membrane fuel cell reactors. *J. CO<sub>2</sub> Util.* **2018**, *23*, 152–158.

(63) Seifitokaldani, A.; Gabardo, C. M.; Burdyny, T.; Dinh, C.-T.; Edwards, J. P.; Kibria, M. G.; Bushuyev, O. S.; Kelley, S. O.; Sinton, D.; Sargent, E. H. Hydronium-Induced Switching between CO<sub>2</sub> Electroreduction Pathways. *J. Am. Chem. Soc.* **2018**, *140*, 3833–3837.

(64) Reinisch, D.; Schmid, B.; Martić, N.; Krause, R.; Landes, H.; Hanebuth, M.; Mayrhofer, K. J. J.; Schmid, G. Various CO<sub>2</sub>-to-CO Electrolyzer Cell and Operation Mode Designs to avoid CO<sub>2</sub>-Crossover from Cathode to Anode. *Z. Phys. Chem.* **2020**, *234*, 1115–1131.

#### ■ NOTE ADDED AFTER ASAP PUBLICATION

This paper was published on October 27, 2020, before all final corrections were made. The corrected version was reposted on November 6, 2020.